NANO · MICRO small
www.small-journal.com

Surface Modification of Transition Metal Dichalcogenide Nanosheets for Intrinsically Self-Healing Hydrogels with Enhanced Mechanical Properties

Chirag R. Ratwani, Shengxi Zhao, Yi Huang, Mark Hadfield, Ali Reza Kamali, and Amr M. Abdelkader**

Nanocomposites with enhanced mechanical properties and efficient self-healing characteristics can change how the artificially engineered materials' life cycle is perceived. Improved adhesion of nanomaterials with the host matrix can drastically improve the structural properties and confer the material with repeatable bonding/debonding capabilities. In this work, exfoliated 2H-WS_2 nanosheets are modified using an organic thiol to impart hydrogen bonding sites on the otherwise inert nanosheets by surface functionalization. These modified nanosheets are incorporated within the PVA hydrogel matrix and analyzed for their contribution to the composite's intrinsic self-healing and mechanical strength. The resulting hydrogel forms a highly flexible macrostructure with an impressive enhancement in mechanical properties and a very high autonomous healing efficiency of 89.92%. Interesting changes in the surface properties after functionalization show that such modification is highly suitable for water-based polymeric systems. Probing into the healing mechanism using advanced spectroscopic techniques reveals the formation of a stable cyclic structure on the surface of nanosheets, mainly responsible for the improved healing response. This work opens an avenue toward the development of self-healing nanocomposites where chemically inert nanoparticles participate in the healing network rather than just mechanically reinforcing the matrix by slender adhesion.

1. Introduction

Dispersion of nanomaterials within the polymeric matrix of composites has always been challenging due to intrinsically strong interactions between nanofillers. This has attracted enormous attention in the modification of nanomaterials to make their dispersion easier by increasing the interaction between the individual nanoparticles and the host matrix. The enhancements that nanomaterials are supposed to offer to the matrix are hardly ever approaching the theoretical values due to several factors such as aggregation of nanoparticles, the defects introduced during the nanomaterials preparation, and even the lateral size of the particles. It is only when large lateral dimensions of the nanofillers are used, chemical bonding with the matrix and thorough dispersion through the matrix can be achieved, resulting in drastic improvements in the mechanical properties of the host.[1] The homogeneous distribution of the filler is even more crucial when additional properties for smart materials are required, such as conductivity,[2] flame retardancy,[3] and self-healing.[4] For most materials used in engineering applications, the self-healing ability is desirable due to constant loading-unloading effects during their service life. In a typical self-healing process, physical and/or chemical bonding occurs at the cleavage site between the broken chains' reactive ends. Such kind of bonds can either be formed by relatively weaker hydrogen bonding (versatile due to the easy availability of abundant hydrogen donor and acceptor sites on polymeric chains)[5] or by covalent interactions. The latter usually need an external stimulus for rebonding due to the high bond energy of covalent bonds, ≈ 400 kJ mol^{-1} for C—C bonds, which is 10 times higher than that of a typical hydrogen bond energy.[6] Hydrogen bonding interactions between the nanosheets and the polymeric chains provide additional hydrogen bond donor/acceptor sites resulting in a well-connected dynamic bonding network which can be cleaved and amended on demand.

However, the addition of any nanofillers to the matrix, particularly those with low hydrogen donor/acceptor sites, tends

C. R. Ratwani, Y. Huang, M. Hadfield, A. M. Abdelkader
Department of Design and Engineering
Bournemouth University
Talbot Campus
Poole BH12 5BB, UK
E-mail: aabdelkader@bournemouth.ac.uk
S. Zhao, A. R. Kamali
Energy and Environmental Materials Research Centre (E2MC)
School of Metallurgy
Northeastern University
Shenyang 110819, P. R. China
E-mail: ali@mail.neu.edu.cn
The ORCID identification number(s) for the author(s) of this article can be found under https://doi.org/10.1002/smll.202207081.

DOI: 10.1002/smll.202207081

to hinder the healing ability due to the absence of chemical interactions amongst the constituents of the composite.[7] One strategy to improve the healing power of composites is to functionalise the filler with hydrogen donor/acceptor groups. Graphene oxide can be a perfect filler that has been reported to introduce significant enhancements to the polymer matrix, where it can be tuned to vary the content of hydrogen bonding sites.[8] Compared to graphene, 2D transitional metal dichalcogenides (TMD) possess much higher bandgap and better tribological properties; and therefore, the full potential of TMD-polymer composites is yet to be explored. Their unique electronic and lubricating properties would allow them to tune the composite functionality for applications such as electronics,[9] sensing,[10] optoelectronics,[11] energy storage,[12] and conversion.[13] Furthermore, 2D TMDs like MoS_2 and WS_2 have experimentally proven to show exceptional tribological performance (even better than graphene).[14,15] They are of key importance as a solid lubricant or as a lubricant additive to the industry. Therefore, it would be ideal to introduce hydrogen bonding sites on TMDs to make mechanically robust and self-healable polymer nanocomposites for next-generation applications such as self-lubricating surfaces or flexible electronics.

Earlier works in self-healable polymer composites excluded such TMD nanosheets from the healing process[16] or employed alternative healing chemistry.[17] Meanwhile, functionalization attempts for TMDs focused on thiol-ligand conjugation and showed that TMDs, like MoS_2, can be functionalized in the presence of thiols to fill the basal-plane sulfur vacancies and impart bonding sites from the reduced disulfide bonds.[18] This suggests that the simple techniques conventionally used for graphene oxide functionalization can also be used for TMDs, and sulfur vacancies can be substituted by thiol-ligand conjugation. However, in recent studies, the use of organic thiols to impart covalent functionality to TMDs has been criticized,[19] raising concerns about their applications in healable nanocomposites.

In this work, thiol functionalized TMDs were synthesized and studied for the change in their surface properties. As a precedent, surface-modified nanosheets were augmented with a widely studied polymer-based hydrogel (polyvinyl alcohol hydrogel) and studied for their role in self-healing and mechanical reinforcement. Motivated by the improvement in the properties of the hydrogel, it was essential to elucidate the healing mechanism of such composite hydrogels while also investigating the mechanism of TMD modification by organic thiols. To begin with, WS_2 was exfoliated by a modified Li intercalation method using a binary mixture of low boiling-point solvents to provide a facile and non-toxic route for synthesis and prevent the conversion of 2H-WS_2 (semiconductor phase) to 1T-WS_2 (metallic phase). Then, surface modification of the exfoliated WS_2 nanosheets was performed using an organic thiol. Following that, WS_2 nanosheets modified with Dithiothreitol (DTT) were blended with PVA at elevated temperatures to produce a mechanically strong, stable, and non-leaky hydrogel by crosslinking hydroxyl bonding sites present on PVA and the surface of WS_2. The healing properties of the hydrogel under atmospheric conditions and indirect heating by electromagnetic stimulus were studied. The mechanism of healing and surface modification was also investigated using advanced spectroscopic techniques.

2. Results and Discussion

2.1. Characterization of Nanosheet Morphology

The formation of 2D 2H-WS_2 nanosheets via the modified chemical exfoliation was first confirmed by the atomic force microscopy (AFM) analysis. As can be seen from **Figure 1**a,b, the lateral size of the exfoliated nanosheets is large and most of the nanosheets ranged from 600 nm to 1.2 µm. The height profile of the nanosheet is shown in Figure 1c shows 1.5 nm thick nanosheets corresponding to the bilayer flakes. There are sheets of all thicknesses mostly to 8 nm, suggesting most WS_2 flakes are less than 10 layers. The statistical analysis shown in the histogram (Figure 1d) indicates that 70% of the flakes are less than five layers (each layer corresponding to ≈0.8 nm according to the literature[20]). Most of the measured larger flakes are amongst the thinnest from the lot. This is very useful for nanocomposites since fillers with high aspect ratios were reported to have a positive impact on the mechanical strength of nanocomposites.[1]

HR-TEM was used to further understand the exfoliated nanosheets' morphological structure. As evident from the low-magnification bright field TEM micrographs of exfoliated WS_2 nanosheets in Figure 1e,f, nanosheets of larger lateral size are present. Furthermore, Figure S1a, Supporting Information, shows the edge of the nanosheet with an internal angle of 120°. Most of these nanosheets have single crystalline features as highlighted from the edge of the nanosheet. Energy dispersive spectroscopy (EDS) mapping recorded on Figure S1a, Supporting Information, as shown in Figure S1b,c, Supporting Information, displays no change in the elemental distribution of the nanosheets. The HR-TEM image revealed light stacking of WS_2 (002) layers with an Interplanar spacing of 0.62 nm and periodic arrays of (100) planes with a spacing of 0.27 nm. Using HR-TEM imaging, some amorphous areas on the edges and Moire pattern due to the nanosheet alignment in the top left part of Figure 1g can also be detected. In the planar orientation, lattice fringes along (100) and (110) planes of the hexagonal WS_2 are also observed. As expected from the harsh chemical-assisted liquid phase exfoliation (LPE) synthesis method, some S-vacancies were observed at the edges, as shown in Figure 1h. However, more vacancies were difficult to detect as antisite defects are more common on TMDs and they tend to have defect energies more than 10 times smaller than the vacancy energies. Notably, the TEM micrograph's Fast Fourier transform (FFT) in Figure 1i shows a clear hexagonal lattice arrangement, pointing toward the semiconductor type of 2H-WS_2 nanosheets. The spots in the FFT of the micrograph are representative of the (100) crystalline planes of the hexagonally oriented 2H-WS_2 lattice. The overlay of the 2H-WS_2 lattice structure on a zoomed-in HR-TEM image confirms the atomic layout of the nanosheets, as shown in Figure 1j.

X-ray diffraction (XRD) analysis was employed to confirm the exfoliation of bulk WS_2 micro powder, as shown in Figure S2, Supporting Information. The sharp characteristic peaks of bulk WS_2 can be identified using lattice parameters a = 3.1532 Å and c = 12.323 Å (ICDD PDF Card No. 08–0237), and the strong peak at 14.59° of 2θ corresponding to (002) plane with a d-spacing of 0.62 nm is used to confirm the 2H phase of WS_2.

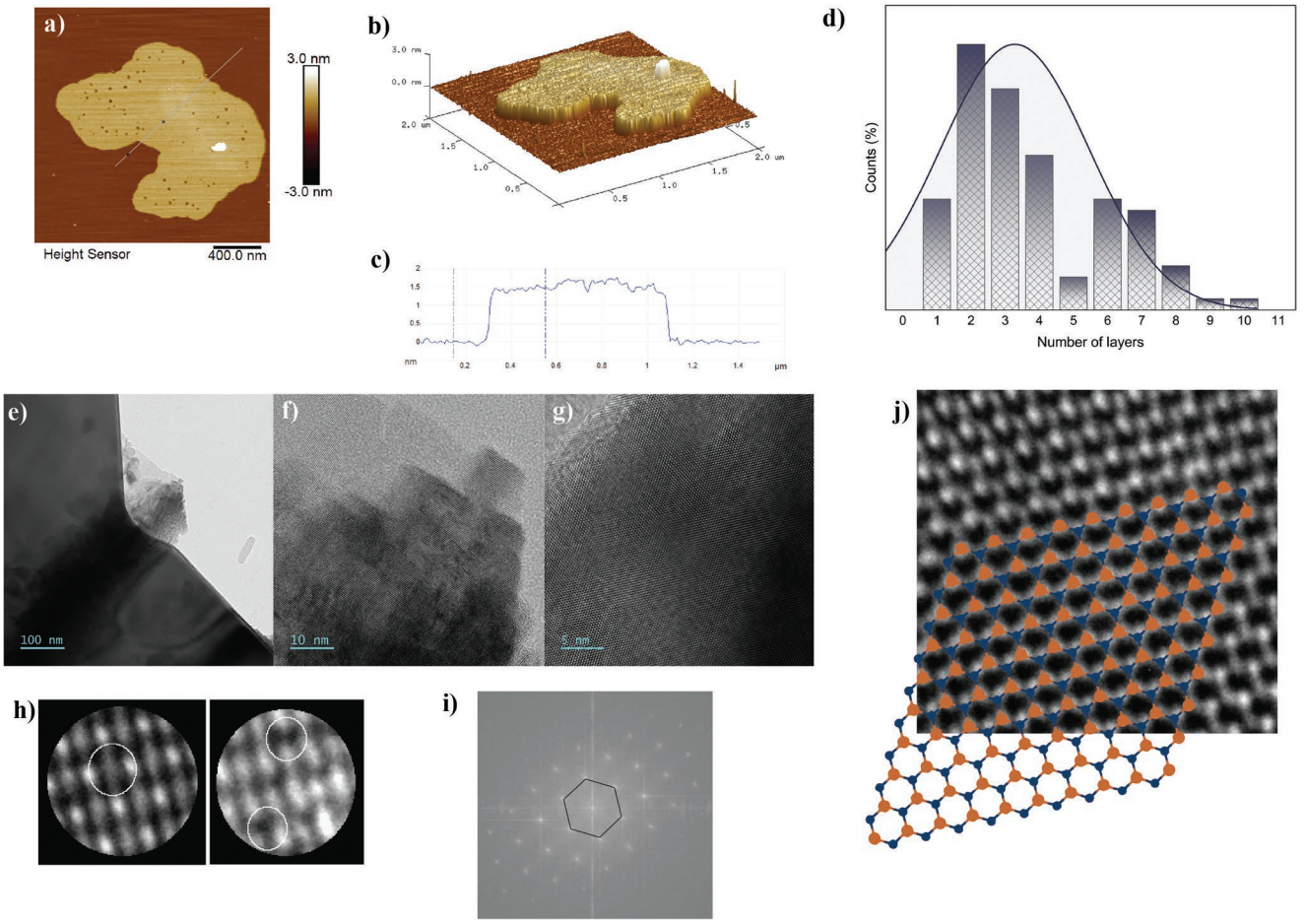

Figure 1. AFM images of WS_2 nanosheets. a) AFM image, b) 3D profile, c) height profile analysis of the nanosheet, d) statistical distribution according to the number of layers in exfoliated nanosheets ($n = 30$), e) low magnification TEM images of exfoliated nanosheets, f,g) HR-TEM images showing transparent nanosheets and crystal fringes, h) high-resolution transmission electron microscopy (HR-TEM) images showing S-vacancy defects on the basal plane, i) fast fourier transform of TEM micrograph with ahexagonal structure, and j) atomic lattice structure of 2H-WS_2 overlay on the TEM micrograph.

As expected after exfoliation, size-related broadening of peaks in the XRD profile of exfoliated WS_2 indicates successful exfoliation of nanosheets. Furthermore, the position of the peak corresponding to the (002) plane is still at the same position (14.59°), suggesting WS_2 maintained the 2H semiconductor phase after exfoliation, in agreement with the literature.[21] Interestingly, other peaks originating from (004) and (006) diminish significantly in size, while (008) and (0010) planes which are prominent in the XRD of the bulk material, disappear for the XRD of exfoliated material which further affirms the formation of nanosheets.

2.2. Characterization of Thiol-Modified WS_2 Nanosheets

The modified Li-intercalation method for exfoliation of WS_2 is used, which produces 2H-WS_2 nanosheets using non-toxic and low-boiling solvents. As this method involves sonication, although mild, it is bound to have some basal plane defects that could act as active reaction sites. Cleland's reagent, also known as Dithiothreitol (DTT) was used as an organic thiol to impart hydrogen bonding sites to WS_2 nanosheets, and advanced spectroscopic techniques were used to verify it.

The crystallinity of the materials before and after exfoliation was characterized by Raman spectroscopy. Raman spectra of WS_2 includes two typical characteristic modes of vibrations E^1_{2g} (in-plane mode) and A_{1g} (out-of-plane mode) for W and S atoms, as shown in **Figure 2**a. For commercial bulk WS_2 micro powder, $E^1_{2g}(\Gamma)$ and $A_{1g}(\Gamma)$ peaks are observed at 353.7 and 419.8 cm^{-1}, respectively. For the exfoliated WS_2, peaks shift to lower wavenumber (by ≈2.6 cm^{-1}) due to an increased lattice stiffening and reduced stacking in the c-direction. Furthermore, the intensity ratio of the $E^1_{2g}(\Gamma)$ peak to $A_{1g}(\Gamma)$ peak changes from 0.798 for bulk to 1.186 for exfoliated materials, which indicates successful exfoliation.[22] Additionally, there are second-order phonons, among which 2LA(M) and 2LA(M)-$2E^2_{2g}$(M) are particularly affected here.

It has been previously confirmed that the intensity increase of the 2LA(M) mode corresponds to an increase in material thickness.[23] As seen from Figure 2a, the 2LA(M) hump can be distinguished in the Raman spectrum of the bulk material with higher intensity than that of the exfoliated WS_2. Similarly,

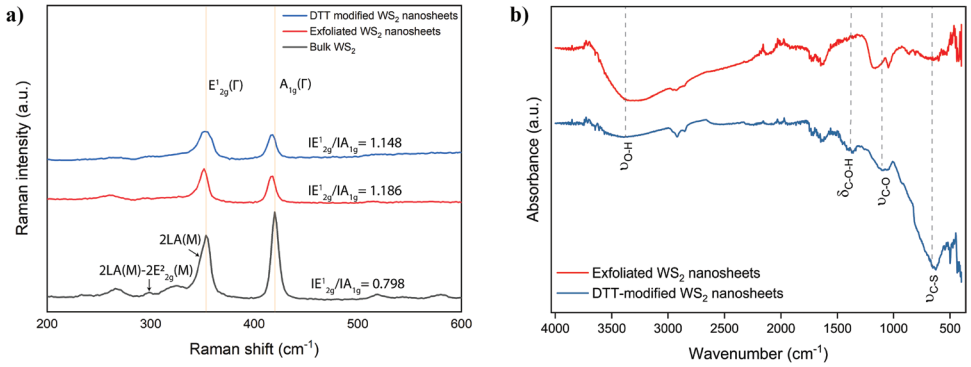

Figure 2. Raman and FT-IR spectra of the samples. a) Raman spectra of Bulk, exfoliated, and DTT-modified WS_2 nanosheets. b) FT-IR spectra of exfoliated and DTT-modified WS_2 nanosheets.

2LA(M)-$2E^2_{2g}$(M) mode has a pronounced peak in the spectrum for bulk material but almost diminishes when observed for its exfoliated counterpart. When it comes to thiol functionalized WS_2, the intensity ratio of the $E^1_{2g}(\Gamma)$ peak to the $A_{1g}(\Gamma)$ peak decreases to 1.148, and a softening of the $E^1_{2g}(\Gamma)$ peak is also observed. Additionally, an increase in the 2LA(M) peak can be observed, which can be used as a criterion to analyze defects in the nanosheets.[24] Since thiol-ligand conjugation alters the S vacancies in the basal plane, a simultaneous increase in the 2LA(M) peak intensity and intensity ratio of $E^1_{2g}(\Gamma)$ peak to $A_{1g}(\Gamma)$ peak indicates a change in the electronic property and defects of the nanosheets. This increase can be attributed directly to the change in the atomic configuration brought in by the functionalization process.

Fourier transform infrared (FTIR) spectra of exfoliated nanosheet show typical features of WS_2 in Figure 2b, indicating that overall vibrational properties have not been alerted by the exfoliation. However, the IR spectrum for DTT-modified WS_2 shows a few interesting new features that could be attributed to thiol-assisted surface treatment. A strong stretching vibration peak of the C—S bond can be observed at 625 $cm^{-1,}$ which can be attributed to thiol-based moieties on the WS_2 surface. The weak S—H stretching in the range of 2600–2550 corresponding to thiol molecules could not be observed in the IR spectra, indicating some changes in the chemical nature of thiol.[25–27] The disappearance of the S—H bonds could be explained by the possible reaction between thiol with the TMDs or a chemical transformation catalyzed by the defects-generated active sites on WS_2 nanosheets. The medium bending bands present in the IR spectra of DTT-modified WS_2 nanosheets at 1368 cm^{-1} suggest the presence of C—O—H bonds after functionalization. A strong C—O stretching at 1040 cm^{-1} also points toward this anomaly. Detecting these C—O bonds, in addition, to confirming some oxygen-containing groups, suggests the thiol derivatives might be linked to the WS_2 nanosheet through some oxides on their surface.

The chemical interaction of DTT and WS_2 was further discerned using X-ray photoelectron spectroscopy (XPS). XPS affirms that the 2H phase of WS_2 nanosheets is retained after exfoliation and remains unchanged even after modification with DTT. This is mainly due to the functionalization technique employed since most other covalent functionalization reported earlier have resulted in polymorph transformation to the 1T metallic phase.[28] As seen from the XPS survey scan in **Figure 3**a,e, no new elements are introduced into the system after DTT modification. The detection of carbon on the non-functionalized WS_2 could be attributed to some residues from the exfoliation solutions or impurities from atmospheric carbon. Oxygen is commonly observed on the surface of TMDs, both on bulk crystals or 2D nanosheets mainly due to partial surface oxidation. This can be seen in the O 1s XPS spectrum of exfoliated nanosheets in Figure S3, Supporting Information. After the modification, clear changes can be observed in the bonding between the elements. The high-resolution spectrum of W 4f in Figure 3b,f shows that the W—O peak at 36.1 eV disappears after DTT-modified WS_2 nanosheets. This could be due to DTT's role as a reducing agent, thereby reducing the photoinduced atmospheric surface oxidation of the WS_2 polymorph. However, there is a slight change observed in W 4f5/2, W 4f7/2, and W 5p3/2 peaks at 38.8, 35.2, and 33.2 eV, respectively, suggesting that DTT atoms could have altered the sulfur vacancies as postulated earlier. S 2p spectrum scan of exfoliated non-functionalized nanosheets in Figure 3c shows the presence of typical S 2p3/2 and S 2p1/2 doublet at 163.5 and 162.1 eV from WS_2 nanosheets. In addition to these peaks, the DTT-modified WS_2 S 2p XPS spectra in Figure 3g show another doublet for the S 2p2/3 and S 2p1/3 at 164.1 and 163.2 eV, respectively, corresponding to C—S bonds introduced by the thiol functionality. Additionally, S-content on the surface increases from 24.48 to 27.45 at% due to DTT modification. The C 1s spectra of both samples give a better idea of the bond formation. C 1s scan of the non-functionalized exfoliated in Figure 3d sample shows the presence of carbon surface contamination. When the C 1s scan of DTT-modified nanosheets is deconvoluted as shown in Figure 3h, it reveals a few interesting bonding characteristics. The increase in the intensity and the slight shift of the C—O peak suggest the hydration of the carbon sites to form C—O—H bonding. The peak at 285.1 eV corresponds to C—S bonding from the thiol agent. Since originally, DTT used for modification does not possess any oxygen-based functional groups, it is possible that DTT got oxidized in the presence of TMD nanosheets and formed an energetically favored six-membered cyclic disulfide of *trans*-4,5-dihydroxy-1,2-dithiane by intramolecular cyclisation. This would also explain the appearance of C—O—H bending and C—S stretching vibration observed in IR spectroscopy.

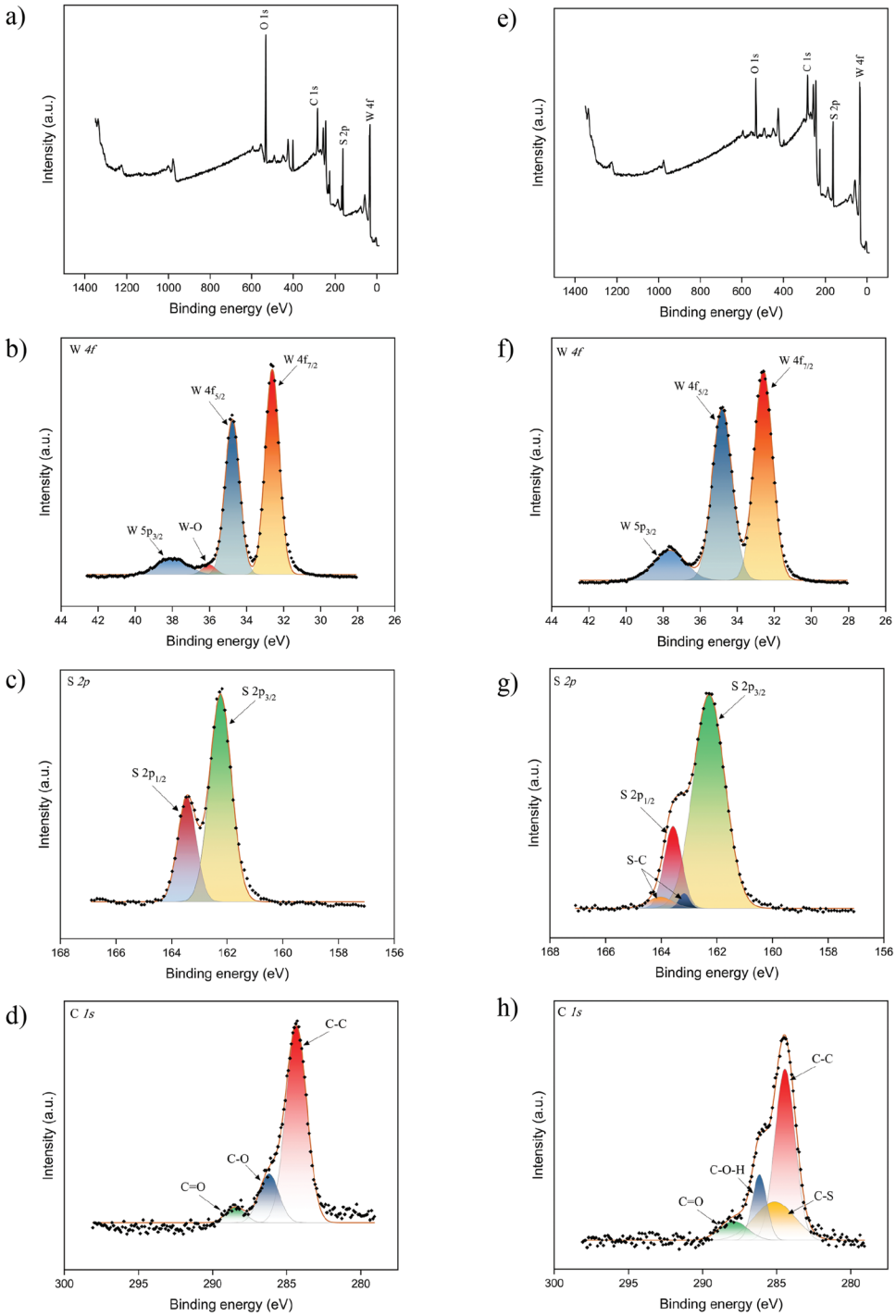

Figure 3. XPS spectra of Exfoliated WS_2 nanosheets. a) Survey scan, b) W 4f-core level, c) S 2p-core level, d) C 1s-core level and XPS spectra of DTT-modified WS_2 nanosheets, e) survey scan, f) W4f-core level, g) S 2p-core level, and h) C 1s-core level.

To further verify our hypothesis, we compared the transmittance IR spectra of thiol-modified WS_2 nanosheets to the IR spectra of DTT (measured) and IR spectra of *trans*-4,5-dihydroxy-1,2-dithiane, also known as oxidized DTT (from literature). The IR spectrum of *trans*-4,5-dihydroxy-1,2-dithiane obtained from the literature is shown in Figure S4, Supporting Information.[29] Comparison of the spectra reveals the presence of some important *trans*-4,5-dihydroxy-1,2-dithiane peaks on the thiol-modified nanosheets while a key R—SH bond stretching corresponding to thiols is present in DTT (as obvious) but absent from *trans*-4,5-dihydroxy-1,2-dithiane and thiol-modified nanosheets. Undoubtedly, from the IR spectra comparison in Figure S5, Supporting Information, the transmittance spectrum of thiol-modified nanosheets is a

better match to *trans*-4,5-dihydroxy-1,2-dithiane as compared to DTT.

The presence of oxygen in the bonds raises several questions, whether the oxidation of DTT is due to the presence of atmospheric oxygen? Also, without atmospheric oxygen, would the reaction form DTT on WS_2 nanosheets or *trans*-4,5-dihydroxy-1,2-dithiane? To answer these, a couple of controlled experiments were performed in which the functionalization was performed in an Ar-filled glovebox with oxygen levels below 12 ppm and after thoroughly deaerating water by bubbling N_2 for 30 min. It was found that oxidation of DTT occurred even in the inert environment, suggesting the oxidation process is mediated either by the solvent or the TMD nanosheets. DTT was then added to 96% ethanol in an inert environment along with WS_2 nanosheets to probe this and it was left stirring for 1 hr. This was mainly to verify the possibility of DTT oxidation in a water-free environment. It was found that DTT was still oxidized and showed similar IR spectra. However, when DTT was stirred in an inert environment with water in absence of nanosheets, C—O—H bending was absent and the presence of R—SH peak at 2570 cm^{-1} could be seen in IR spectra, confirming that WS_2 nanosheets play an important role in oxidation. Thermogravimetric analysis (TGA) of thiol-modified WS_2 nanosheets treated with 6 mg mL^{-1} of DTT solution (Figure S6, Supporting Information) shows a mass loss of ≈ 15% in the range of 170 to 270 °C, typical to the decomposition of thiol-based compounds, suggesting that the mass loss observed is due to the decomposition of attached DTT related moieties. Higher mass loss is observed in samples treated with a DTT solution of higher concentration in the same temperature range, indicating a higher density of DTT-based compounds on the surface.

Remarkably, DTT modification also brought an exciting change in the surface properties of the WS_2 nanosheets. Exfoliated 2H-WS_2 nanosheets, which ordinarily do not redisperse in water, now form a stable aqueous suspension after functionalization, as can be seen in Figure S7a, Supporting Information. The stable water suspension is beneficial for fabricating hydrogel with a water-soluble polymer, as in the case of PVA hydrogels, opening doors for developing an organic solvent-free method for composites preparation. Zeta potential and UV–vis spectroscopy were used to further investigate the surface properties of the thiol-modified nanosheets. Figure S7b, Supporting Information, shows zeta potential measurements of exfoliated nanosheets before and after functionalization. Interestingly, the thiol-modified nanosheets have a less negative zeta potential than non-functionalized nanosheets, suggesting the suspension stability is by stearic stabilization rather than electrostatic repulsion. A change in optical properties accompanied the alteration of surface change. Stable suspensions of nanosheets before functionalization were greyish-black in color. In contrast, the suspension after functionalization is yellowish green, as can be seen in Figure S7a, Supporting Information. UV–vis spectra show the typical characteristics of WS_2 nanosheets in Figure S7c, Supporting Information, with two peaks at ≈640 and ≈544 nm. These peaks correspond to the A1 and B1 direct excitonic transitions of WS_2 originating from the energy split of the valence band and confirming that WS_2 maintained their 2H phase after exfoliation and functionalization. Interestingly, the B1 peaks weaken and undergo a blue shift after functionalization. A similar observation was reported before with graphene and carbon nanotubes after they underwent a polymeric wrapping-like process.[30,31] The wrapping-like phenomenon explains the decrease of the surface charge and further suggests the DTT functionalization stabilizes the nanosheets in water by the stearic effect.

The morphology of DTT-modified nanosheets was further studied using AFM. It was found that it is much easier to obtain monolayer 2H-WS_2 nanosheets after thiol modification mainly due to additional stabilization bought in by attached thiol-based moieties. Suspension in water was allowed to rest for 24 h and the supernatant was drop cast on a smooth mica sheet to prepare the sample for AFM. Remarkable selectivity of laterally-large monolayer nanosheets can be observed in **Figure 4**a,b which makes it much more useful for use in composites. As shown in Figure 4c, the height profile of multiple nanosheets on the mica sheet reveals an average height of 1.3 nm, which is higher than the thickness of monolayer 2H-WS_2 nanosheets. This increase in height caused by functionalization was closely studied by focusing on a single nanosheet, shown in Figure 4d,e. Ridges present on the surface were studied using Peakforce mode to reduce the possibility of tip contamination by organic matter. Ridges have a rather uneven surface morphology suggesting adherence of thiol-based groups instead of nanosheet stacking. Moreover, edge analysis of the nanosheets as shown in Figure 4f stipulates a striated pattern rather than a step-like pattern which would be expected from stacked nanosheets. The sharp slope of hill-like features as compared to the step-like morphology of just exfoliated nanosheets (shown in Figure 1b) is a clear indication of the presence of organic molecules on the nanosheets. HR-TEM micrographs shown in Figure S8a,b, Supporting Information, indicate that functionalization does not alter the lattice structure of nanosheets, although thiol-based moieties were removed during the electron microscopy under the influence of the focused electron beam irradiation.

2.3. Self-Healing in Nanocomposite Hydrogels

The freeze-thaw process was used to synthesize PVA nanocomposite hydrogels by physical crosslinking methods. Control samples of hydrogels with only PVA (PVA), pristine WS_2 nanosheets (PVAW), DTT-modified WS_2 (PVAFW), and hydrogels with DTT-modified WS_2 nanosheets soaked after synthesis in 0.3 M Ammonium sulfate solution (APVAFW) were also studied. To analyze the physical characteristics of the hydrogel, gel fractions (GF) and equilibrium swelling ratios (ESR) for PVAFW hydrogels were measured using standard gravimetric techniques. It was observed that GF increased from 87.3% to 96.7% by increasing the PVA concentration from 10% to 30%, as shown in Figure S9a, Supporting Information. This suggests that denser hydrogels can be obtained by increasing the PVA concentration, which is expected from such hydrogels. ESR values of the hydrogels showed an inverse relation to the concentration of PVA. ESR decreased from 207.2% for 10 wt% PVAFW hydrogels to 191.8% for 30 wt% PVAFW hydrogels, as shown in Figure S9b, Supporting Information, indicating a clear change in hydrogel mesh size.

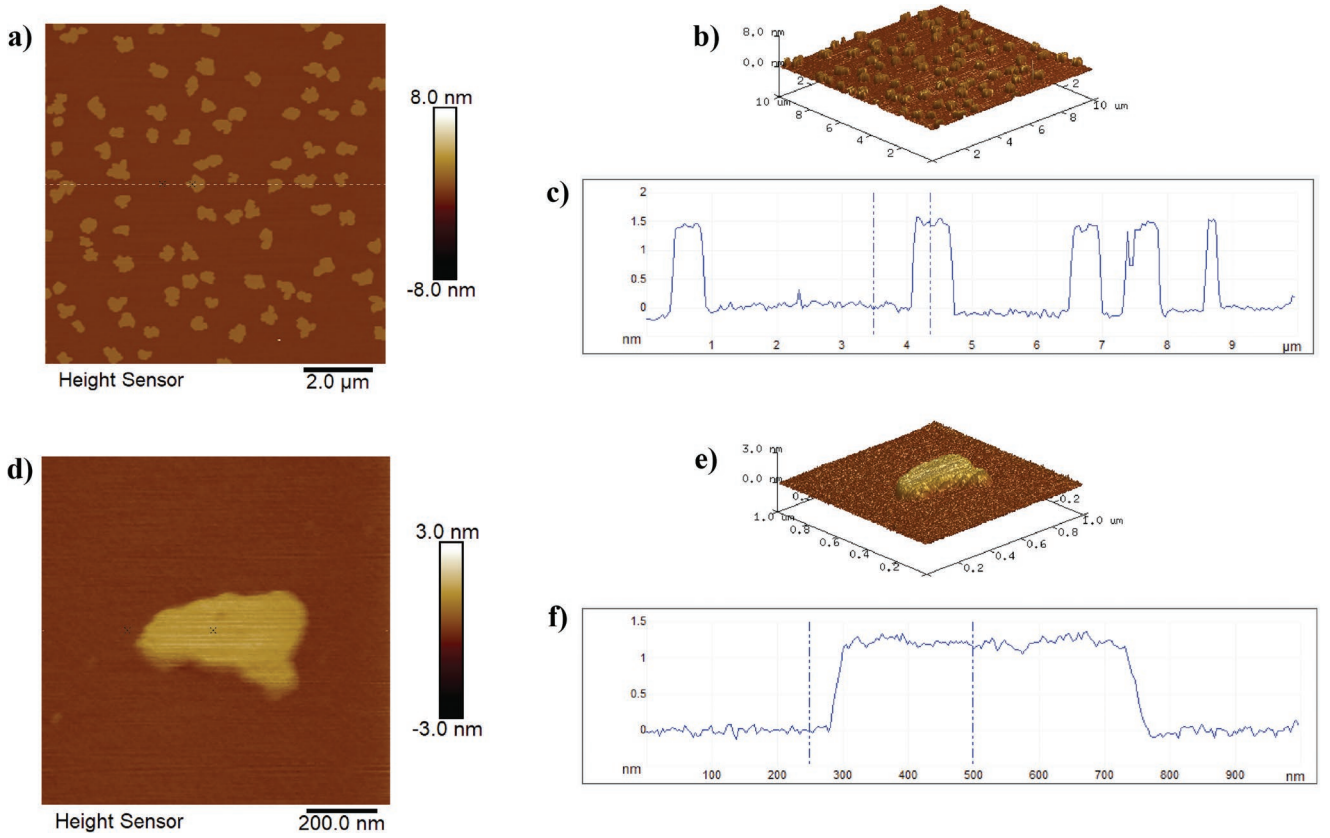

Figure 4. AFM images for thiol-modified 2H-WS_2 nanosheets. a) Typical nanosheets with thickness ≈1.3 nm. b) 3D AFM image of the distribution on mica substrate. c) Height profile for multiple nanosheets. d) Magnified single thiol-modified 2H-WS_2 nanosheet. e) 3D AFM image of a single nanosheet. f) Height profile of a single nanosheet.

Before analysing the self-healing properties of the PVAFW hydrogels, it was important to get an idea about their processability. Hydrogels possess excellent processability and can be twisted to 360° and cast into a thin film with a thickness of 670 µm, as shown in Figure S10, Supporting Information. Then the self-healing performance of the nanocomposite hydrogels under ambient and accelerated healing conditions was characterized. The accelerated healing was triggered by microwave heating and NIR photothermal conversion. As shown in **Figure 5**, PVAFW hydrogels with chemically modified WS_2 possess fast healing characteristics. The hydrogels were cut into two pieces using a super sharp stainless-steel blade to cause the fracture, and healing was initiated by placing the cleaved pieces together. For healing at ambient conditions, cleaved pieces were kept together using mild pressing force for 4 h to allow the healing process to reach equilibrium. Healing using microwave energy was performed in a domestic microwave (800 W) for 60 s, and the time was measured when the magnetron initiated actual irradiation. Similarly, spot healing under NIR light was done by exposing the cleaved surface to a NIR laser (785 nm, 350 mW) for 5 min at room temperature. Figure 5a,b shows autonomous healing at the macroscopic and microscopic levels, while Figure 5c shows healing using accelerated conditions.

The tensile strength of pristine and different WS_2-modified hydrogels was measured to quantify the self-healing ability. The results of the tensile tests are shown in **Figure 6**a. Pure PVA hydrogels have a tensile strength of 261.4 kPa and possess the self-healing ability (23.06% of the tensile strength was recoverable after healing). PVAW hydrogels prepared using pristine WS_2 nanosheets show a much higher tensile strength of 636.3 kPa, due to the reinforcement of polymeric chains by WS_2 nanosheets. This value is significantly higher than hydrogels with graphene oxide as filler material.[32,33] However, PVAW exhibits a lesser ability to self-heal. Only 18.76% of the original tensile strength could be recovered, mainly due to hindrance in polymeric chain movement caused by nanosheets in the matrix. The tensile strength increases by 18%, reaching 748.5 kPa when DTT-modified WS_2 is used as the filler due to the enhanced adhesion with the matrix. Also, adding thiol-modified WS_2 to the matrix significantly increases Young's modulus of the hydrogel, making it much more resistant to deformation than pure PVA hydrogel. Interestingly, the self-healing efficiency rises to 72.83%, emphasizing the role of additional hydrogen bonding sites in reconnecting the broken polymeric chains. Soaking the fresh hydrogels in ammonium sulfate solution yields a hydrogel network with a higher density of hydrogen bonds, giving a better healing efficiency of 89.92%, as evident by Figure 6b. As shown in Figure 5b, broken hydrogel pieces reconnected readily when the healing was observed under an optical microscope. Improvement in the healing efficiency could be attributed to the dynamic nature of junctions in the hydrogels caused by hydrogen bonding

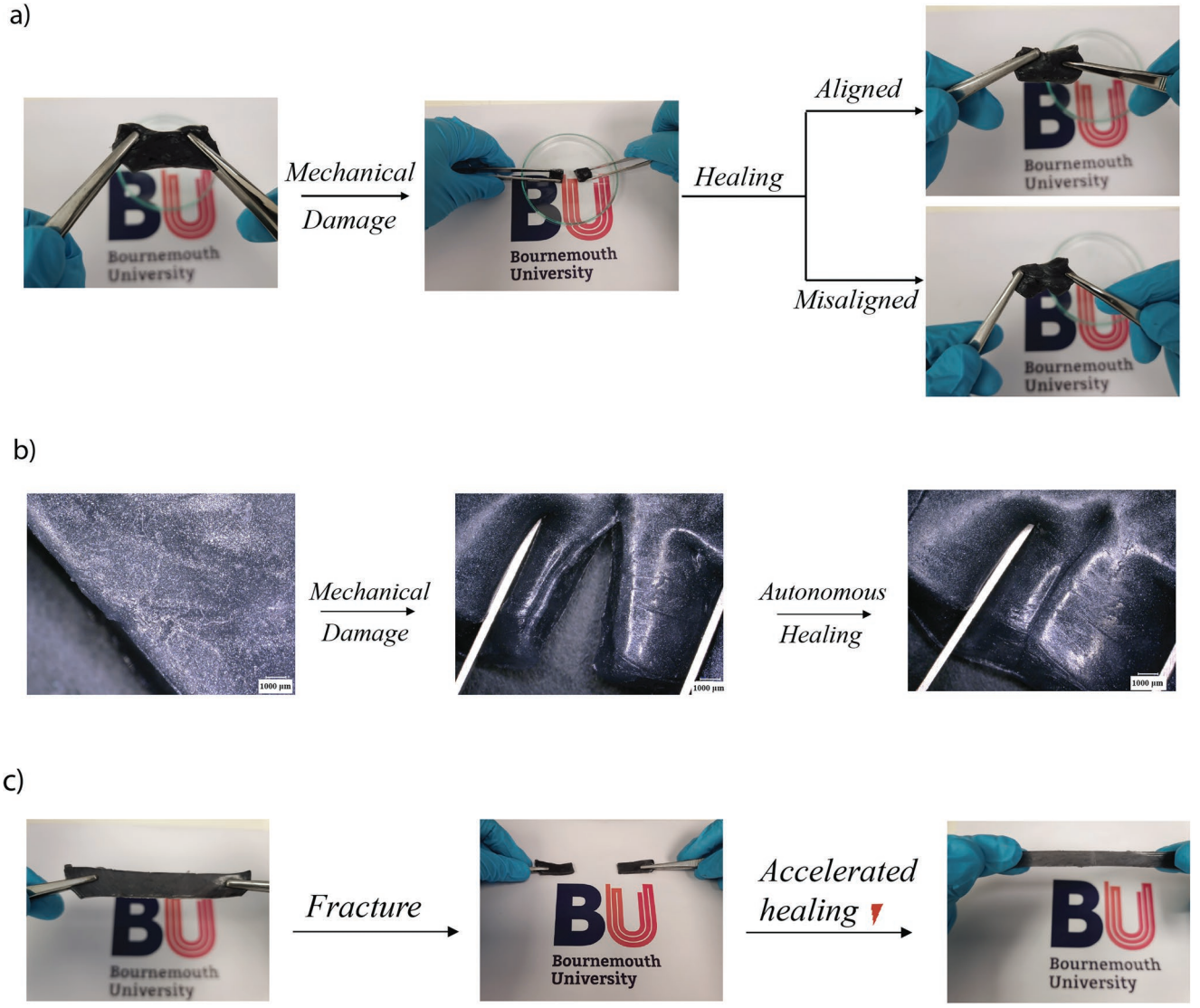

Figure 5. Healing of PVAFW hydrogel. a) Macroscopic image. b) Microscopic image. c) Healing in accelerated conditions.

between the PVA chains, functionalized WS_2, and ammonium sulfate ions. The self-healing properties arose from the H-bonding interaction between PVA chains-functionalized WS_2-ammonium sulfate and physical interactions caused by the entanglement of PVA chains and WS_2 nanosheets. Water medium is essential to dissolve PVA, provide chain mobility to the polymeric chains and assist in H-bond formation, while ammonium sulfate within the solvent serves as additional junction points to further enhance the density of H-bonds. However, as expected for such hydrogels, 100% recovery of tensile strength is not observed, mainly due to damage in the polymeric backbone during cleavage and probably due to improper aligning of reactive chain ends when the two pieces were put together. Also, as this hydrogel is a soft material, even a very sharp blade tends to slightly bend the surface rather than giving a smooth cut interface. The slight bending causes some of the free reactive ends, freshly created by fracture, to reconnect within the same side of the cut, preventing the nanocomposite hydrogel from achieving 100% healing efficiency. The healing efficiency and tensile strength of various samples are compared in Figure 6c. A high healing efficiency of 98.2% and 93% could be achieved when accelerating the healing using microwaves or NIR laser, respectively. It also takes a shorter time to complete this high level of recovery (60 s for the microwave-treated samples and 300 s for the NIR laser), thanks to the excellent photothermal conversion and microwave absorption properties of WS_2 nanosheets. Healing efficiency is compared in Figure 6d after healing using different techniques. Both microwave and photothermal healing facilitate the H-bond formation by the thermally induced motion of polymeric chains resulting in chain slippage, cleavage, and reformation at the rupture surface. Furthermore, issues arising from improper alignment of polymeric chains become less significant since new bonds are formed on the newly created interface by the large number of chain arrangements induced by the thermal motions. It is also interesting to note that out of five samples taken for tensile test

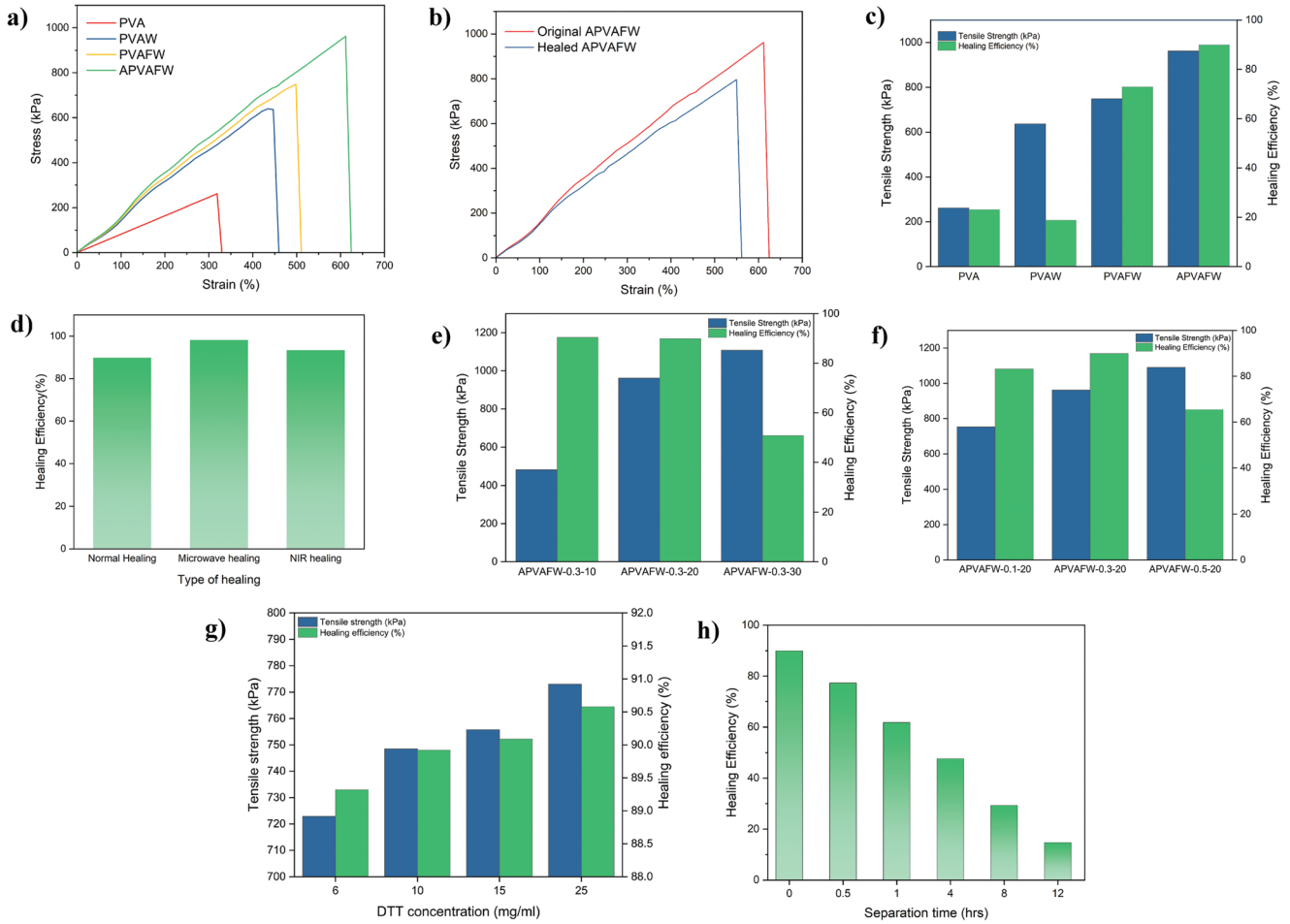

Figure 6. Mechanical and/or healing properties. a) Stress-strain graphs of different hydrogel samples. b) Stress-strain graph for Virgin and healed hydrogel. c) Comparison of healing efficiency and tensile strength of different hydrogels. d) Effect of accelerated healing. e) Effect of change in PVA concentration with WS_2 content constant at 0.3 wt%. f) Effect of change in nanosheet concentration with PVA content constant at 20 wt%. g) Effect of change in DTT concentration during functionalization. h) Effect of separation time.

after healing, the fracture point after healing for two samples differed from the original fracture surface. This would suggest that microwave heating of hydrogel causes higher movement of PVA chains and might compromise the integrity of the hydrogel if not controlled appropriately.

To gain better insights into the effect of various components on the mechanical and self-healing properties, further tests were performed by changing the composition of the hydrogels. The tensile strength of hydrogels with fixed WS_2 content of 0.3 wt% increased from 450 kPa to over 1100 kPa with increasing the PVA concentration in the hydrogel from 10% to 30%. The healing efficiency shows a slight decrease of 0.53% when the PVA loading is doubled to 20%. It is only at the high PVA loading that the healing efficiency significantly dropped from 89% to about 50%, probably due to the restricted chain mobility in the denser hydrogels. Our results show optimal strength and healing efficiency at 20% concentration out of the three concentrations that were tested. It should also be noted that it was onerous to obtain a homogenous solution with PVA concentrations higher than 30%; hence, only 10–30% concentrations have been considered for this study and compared in Figure 6e.

Increasing the functionalized nanosheet loading from 0.1% to 0.3% results in tougher hydrogels and an increase in healing efficiency, as seen in Figure 6f. However, increasing the thiol-modified WS_2 loading from 0.3% to 0.5% plummets the healing efficiency from 89.92% to 65.46%. The decrease in the healing efficiency at a high loading of functionalized WS_2 could be because the increase in H-bonding sites offered by modified WS_2 is overpowered by hindrance in the chain mobility caused by a large concentration of the nanosheets in the matrix. This was further confirmed by changing the amount of organic thiol during the surface modification of WS_2. When fixing the WS_2 content at 0.3 wt% but increasing the level of DTT on the nanosheets, the healing efficiency significantly increases, reaching a value of 90.6% as shown in Figure 6g. It can also be seen that the increase in DTT concentration that occurred during the modification process also results in stronger hydrogels due to better bonding characteristics arising from an increase in H-bond acceptor and donor sites. These results suggest that the role of DTT functionalization is more crucial to the healing process than the content of nanosheets in the composites. It should be noted that hydrogels could not heal

autonomously when low DTT concentration was used for functionalization.

Healing hydrogels after keeping the cleaved pieces separated for a considerable time has always been challenging. The main reason for this decline in the healing ability is due to the tendency of H-bond acceptor sites to find the nearest H-bond donor sites and undergo hydrogen bond formation to minimize the surface energy. As shown in Figure 6h, nanocomposite hydrogel showed excellent self-healing properties, even if the damaged surfaces were kept apart for a long time. Due to the excellent photothermal properties of WS_2 nanosheets, polymer chain rearrangement is facilitated, and rebonding of H-bonds takes place on the interface with a minimal external stimulus. It was also observed here that hydrogel begins to lose moisture by diffusion when kept in a very dry environment. However, PVAFW hydrogels took significantly more time to dry out completely compared to pure PVA hydrogel. The functionalized WS_2 nanosheets could have promoted the chemisorption of water on the surface, which takes longer to be removed from the hydrogel. The denser and highly packed nature of PVAFW hydrogels could have also slowed down the rate of water evaporation. It should be noted that some degree of aggregation of nanosheets in the hydrogel matrix is inevitable due to the nature of the polymer, and similar phenomena have been reported previously in works involving PVA.[34] However, a much lesser degree of aggregation is observed when thiol-modified nanosheets were used for the preparation of the nanocomposite, as evidenced by Raman mapping shown in Figure S11, Supporting Information. Figure S11a, Supporting Information, shows the Raman spectrum of a thin cross-section of dried FWPVA hydrogel, where typical features of WS_2 and PVA are highlighted. 3D representation of Raman mapping in Figure S11b–d, Supporting Information, of corresponding peaks shows the polymer and nanosheets are evenly distributed throughout the measured area. Most points in the matrix have an intensity ratio of the $E^1_{2g}(\Gamma)$ peak to $A_{1g}(\Gamma)$ higher than 1, indicating no or very low aggregation. Some points in the far back have higher $E^1_{2g}(\Gamma)$ peaks which could be due to aggregation. Multiple samples of the same cross-sectional size were analyzed and a similar proportion of aggregation was observed. However, detrimental effects of aggregation could only be observed when WS_2 concentrations higher than 0.3 wt% were used in the matrix, as discussed earlier.

Furthermore, real-time FTIR measurements to further investigate the changes in the chemical bonds during the self-healing process were also conducted. For the as-prepared samples, there is an apparent increase in the −CH stretching at lower wavenumber when DTT functionalized WS_2 is added to the composite, possibly due to additional −CH bonds introduced by the oxidized thiol on the surface of WS_2 nanosheets as clearly visible in Figure S12a–c, Supporting Information. The collected FTIR spectra of the as-prepared PVAFW gels before inducing the cut and during the healing are displayed in Figure S12d–f, Supporting Information. The as-prepared and uncut hydrogel surface has the highest proportion of −OH functional groups (3275 cm^{-1}), which didn't change much for the freshly cut surface. The proportion of C−H and C−O bonds decreases on the freshly cut surface due to the bond breaking. After healing, the intensity of both C−H and C−O recovered as a result of the chain reconnection. On the other hand, the −OH stretching decreases after healing, indicating the participation of hydrogen bonding sites from the *trans*-4,5-dihydroxy-1,2-dithiane cyclic molecule.

2.4. Proposed Mechanism

Modified Li-intercalation exfoliation produces few-layer flakes of 2H-WS_2 with a high aspect ratio, which is vital to impart mechanical strength to the hydrogels. In this approach, Thiol modification alerts the surface chemistry and introduces hydrogen bonding sites to the TMD nanosheets. The thiol modification forms hydrogen bonding between nanosheets and the polymer matrix, improving the adhesion between the nanofiller and the matrix. The strong filler-matrix interface enhances the stress transfer throughout the nanocomposite, improving the mechanical properties of the hydrogel. To achieve such high healing efficiency, it is paramount to optimize the proportion of nanosheets in the matrix to balance between the gain in mechanical strength and loss in healing efficiency, while also enhancing the functional groups on the surface. The abundance of hydrogen bonding sites (two hydrogen donor sites and four hydrogen acceptor sites on each attached molecule of *trans*-4,5-dihydroxy-1,2-dithiane) significantly enhances the healing efficiency and kinetics. The healing mechanism is shown graphically in **Figure 7** and the performance of this nanocomposite hydrogel as compared to the top performers in this domain is shown in Figure S13, Supporting Information. Probing into the functionalization of nanosheets, it was observed that DTT is oxidized in the presence of nanosheets, mainly by reducing the inevitable ambient photoinduced surface oxidation of WS_2. Moreover, increasing the level of DTT functionality on the nanosheet surfaces improves both the mechanical and healing properties. The only viable explanation for this enhancement at this stage is that H-bonding sites increase with the increase in DTT amount, and it appears to be not limited by S-vacancies as very high amounts of DTT have been used. Authors agree with previously published literature that *trans*-4,5-dihydroxy-1,2-dithiane molecules are attracted to those sites due to higher affinity toward S-vacancies as suggested by Sim et Al.[35] and will cause the passivation of active S-vacancies. However, if S-vacancies are unavailable (or already passivated), oxidized thiol molecules could then graft onto the S atom of the 2H-WS_2 nanosheet very likely by chemisorption on the surface. Further studies using ab-initio calculations are recommended for a better understanding of the healing mechanism and to probe into chemical steps involved in the grafting of thiol-based moieties on the WS_2 nanosheet surface. The proposed WS_2 functionalization reaction mechanism is shown graphically in **Figure 8**.

3. Conclusion

Surface modification of WS_2 nanosheets combined with composite formulation with PVA brought about by the facile solution processing result in an intrinsically self-healable hydrogel that can be healed autonomously in a short time. Due to the scrupulous

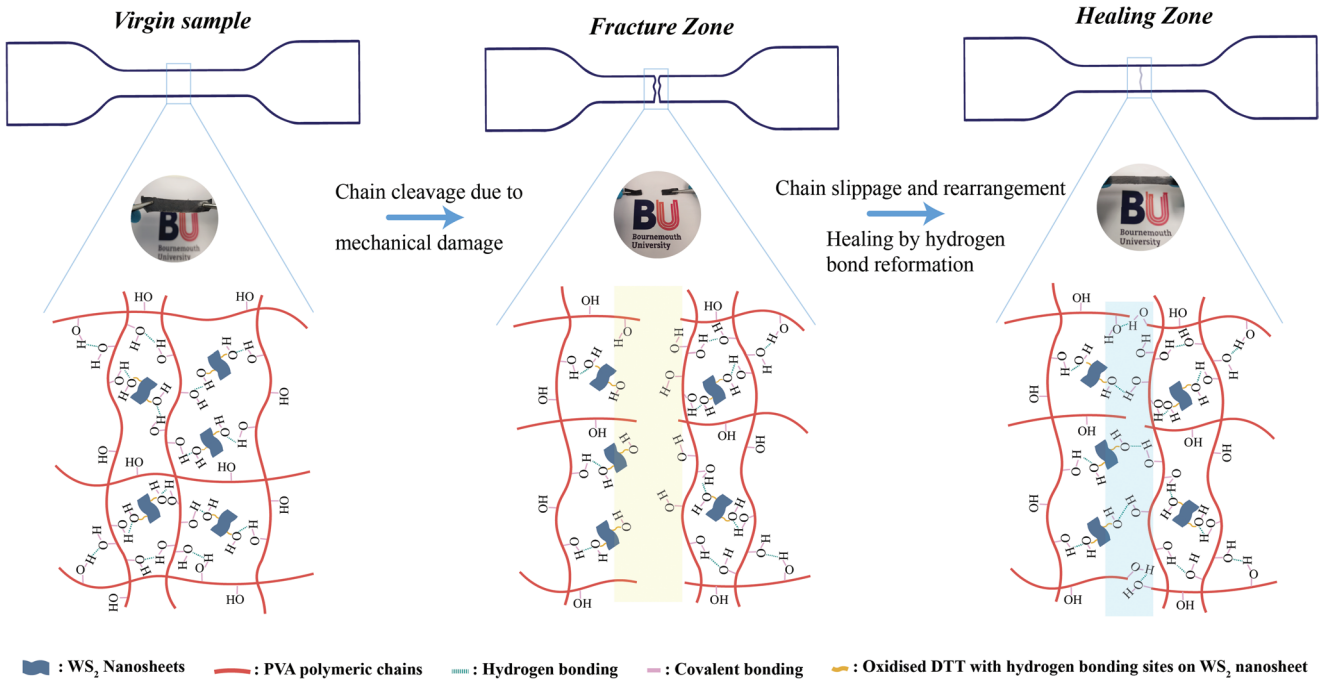

Figure 7. Proposed mechanism of hydrogel healing.

design of the nanocomposite and controlling the proportions of the constituents, hydrogels with excellent mechanical properties and highly efficient self-healing ability could be synthesized. Hydrogels with a nanosheet loading of as low as 0.3 wt% could improve the tensile strength by almost four times with a healing efficiency of 89.92%. Along with improvements in the composite properties, surface modification also yields a remarkable selectivity for laterally-large monolayer nanosheets in water suspension, making their processing much simpler. Probing into the mechanism of healing reveals the formation of a stable cyclic structure on the WS_2 nanosheet surface due to thiol modification, which forms an enhanced hydrogen bond network and reinforces the hydrogel on the molecular level. The effect of different parameters on the healing characteristics yields important information on the contribution of different components to healing dynamics. The present approach provides an effective strategy to incorporate disulfide-based TMDs like WS_2 and MoS_2 into the composite chemistry by chemically binding them to the matrix. This study could open doors for the functionalization of such materials and their use in various intrinsically healable polymeric composites. Such hydrogels have great potential as a highly processable biomaterial or as a component for self-lubricating surfaces with excellent tribological properties of these TMDs, high autonomous healing efficiency, and biocompatibility.

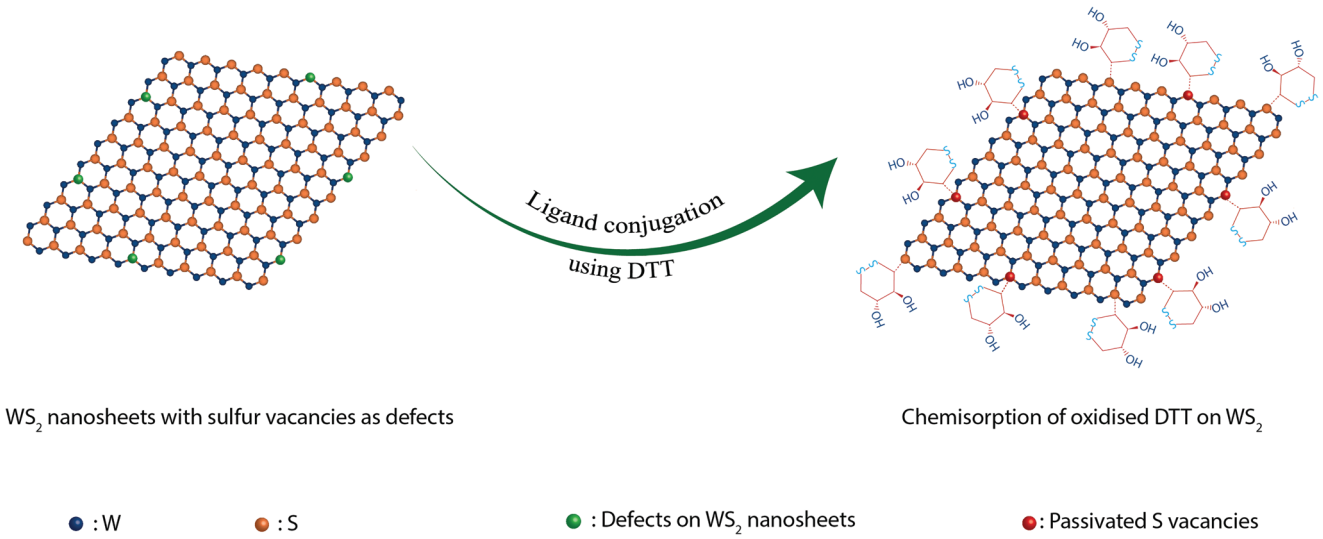

Figure 8. Proposed mechanism of DTT-modification of WS_2 nanosheets.

4. Experimental Section

Materials: Tungsten (IV) sulfide (powder, 2 µm, 99%) and lithium chloride (LiCl, powder, ≥99.98% trace metals basis) were purchased from Sigma-Aldrich. Dithiothreitol (DTT; Cleland's reagent, molecular biology grade) was sourced from Thermo Fischer, UK. Polyvinyl Alcohol (PVA, 98–99% hydrolyzed, Avg. MW 57 000–66 000) and ammonium sulfate were purchased from Alfa Aesar. Isopropyl Alcohol (IPA) (≥99%, Reagent grade) and other solvents were sourced from Fischer scientific. Double distilled water was used for all experiments. All reagents were used as sourced without further purification.

Exfoliation of WS_2 by Modified Chemical Intercalation Method: Single-layer to few-layer WS_2 nanosheets were synthesized using a modified chemical intercalation method (as shown in Figure S14, Supporting Information) to retain the 2H phase of WS_2 and prevent conversion to the 1T phase, inspired from literature.[36] Tungsten (IV) sulfide powder (50 mg) was dispersed in an IPA/water mixture (60 mL, 20% IPA/80% water) with LiCl as the source of lithium halide in a 1:1 mole ratio. The dispersion was sonicated in a low-powered bath sonicator for 60 min. The resulting sonicated dispersion was centrifuged at 9000 rpm for 15 min to remove the unsolved lithium halide. The supernatant was removed, and the sediments were washed with IPA three times to remove the remaining solvated LiCl. Finally, the washed WS_2 was dispersed in an IPA/water mixture (20% IPA/80% water) as this combination has proven to provide maximum yield due to a perfect match between the surface tensions.[37] After the second dispersion, it was sonicated again for 30 min and the sample was dried at 90 °C under a vacuum for 5 h before being used in subsequent experiments.

TMD Nanosheet Functionalization with Organic Thiol: Exfoliated WS_2 nanosheets were dispersed in a 1:1 mixture of ethanol and water. Ethanol helps maintain the optimum pH range (7.1 to 8.5 pH) for effective reduction using DTT. Water was deaerated by purging N_2 gas for 30 min before dissolving DTT to prevent direct oxidation of thiols. DTT solutions of different concentrations were prepared immediately before use and kept in an ice bath till the reaction was initiated. 30 mL dispersion with WS_2 nanosheets (0.1 g) was mixed with 10 mL of DTT solution(s) and stirred for 2 h in a closed inert environment at room temperature. After the reaction was complete, nanosheets were washed with water and lyophilized at −55 °C to dry them. All results were discussed for hydrogels made with WS_2 nanosheets modified using a 10 mg mL^{-1} solution of DTT unless specified. The reaction mechanism explained as per the literature is shown in Figure S15, Supporting Information.

Synthesis of PVA-Based Self-Healing Hydrogels with Functionalized WS_2: PVA-based hydrogels were prepared by the facile freeze-thaw cycling method. For this, the desired amount of PVA (Concentration: 10, 20, and 30 wt%) was dissolved in water at 95 °C, and then WS_2 nanosheets with calculated loading (Concentration: 0.1, 0.3, and 0.5 wt%) were added to the solution. PVA with a higher degree of hydrolysis was used to increase −OH bonding groups making the hydrogen bonding interactions between the polymer and nanosheets more pronounced. PVA of 60 000 MW was chosen mainly to emphasize the effect of surface modification of TMDs and limit the chain entanglement, which is usually very high in PVA with higher MW. Beaker was kept in an oil bath to ensure even heating and covered to prevent water loss. The mixture was then stirred at an elevated temperature (95 °C) for 2 h to obtain a homogenous solution. Next, it was sonicated for 20 min at a high temperature to remove bubbles from the sample. The resultant hydrogel slurry was quickly injected in a dog-bone mould to cast the hydrogel for self-healing and tensile tests. The prepared hydrogel was cooled at −20 °C for 2 h to freeze the hydrogel, followed by thawing at room temperature for 6 h. This cycle was repeated three times for all samples. PVA denotes pristine PVA hydrogels without nanosheets, PVA hydrogels with bare exfoliated nanosheets are denoted as PVAW, and hydrogels with DTT-modified WS_2 nanosheets are denoted as PVAFW. To amplify the effect of functionalization, additional hydrogen bonding sites were introduced into the samples by a salting-out method using 0.3 M ammonium sulfate solution and completely immersing the hydrogel samples for 3 h at room temperature. These samples were denoted by APVAFW.

Characterization: Atomic force microscopy was conducted using a Bruker Dimension Icon device. A transmission electron microscopy (TEM) was conducted using a Tecnai F20 microscope, equipped with an energy-dispersive X-ray detector (EDS), at an accelerating voltage of 200 kV. A fully confocal Horiba XploRA spectrometer (Horiba, Japan) with a green laser (λ = 532 nm) and 50× objective lens was used for Raman spectroscopy and mapping. Tests were conducted under ambient conditions, and parameters for measurement were optimized to avoid fluorescence and obtain a higher signal-to-noise ratio. Infrared spectra were collected using Agilent Cary 360 FTIR spectrometer (Agilent Technologies, USA) with a Diamond ATR module. Powdered X-ray diffraction measurements were performed using Cu Kα radiation with a Siemens D5000 diffractometer (Siemens, Germany). Mechanical testing of materials was carried out using a Universal testing machine Zwick/Roell Z030 (ZwickRoell, Germany) with an Xforce K+ 10 kN load cell and at a constant crosshead speed of 5 mm min^{-1}. TGA analysis was conducted using NETZSCH STA 409 PC/PG under the flow of N_2 at a rate of 5 K min^{-1} in an Alumina crucible. Optical imaging of samples was conducted using Keyence VHX-5000 digital microscope (Keyence Corporation, Japan), and digital photos of the samples were taken using Nikon D5600 (Nikon, Japan). The nanosheets were freeze-dried in HETO LyoPro 3000 (Heto/Holten A & S, Allerød, Denmark). The condenser temperature for drying was −55 °C at the pressure of 2.89 hPa, and the drying time was 72 h. UV–vis spectra were obtained using Agilent Cary 60 UV–vis Spectrophotometer using dispersions in *N*-Methyl-2-pyrrolidone solvent using Quartz cuvettes with 10 mm path length. The healing experiments under microwave irradiation were conducted using a domestic microwave (DeLonghi AM820AGX) at 800 W for 10 s.

Surface characterization was performed on an X-ray photoelectron spectroscopy (XPS, Thermo Scientific). Zeta potentials were measured at a concentration of 0.10 mg mL^{-1} using a Zetaplus analyzer (Litesizer 500, Anton Paar Instruments) by the electrophoresis light scattering method at an adjusted voltage of 200 V. Tensile testing was carried out on dog-bone-shaped hydrogel samples made in accordance with ASTM D412 standards. The tensile stresses were calculated by dividing the maximum applied force by the effective cross-sectional area, and the strain was calculated by measuring the elongation percentage with respect to the initial and final length. Five test specimens were prepared for each sample, and the average was taken as the tensile strength to calculate the healing efficiency.

The dog-bone shaped samples were cut into two pieces, which were brought together to initiate hydrogen bond formation and kept together for 2 h. Healing efficiency was calculated by taking the ratio of the tensile strength of the healed sample to that of the virgin sample. For the accelerated healing experiments, the samples were irradiated in the microwave for seconds and allowed to cool down naturally. Spot healing was also tested using a NIR laser.

Freshly prepared hydrogels were used to determine the values of gel fraction (GF) and equilibrium swelling ratio (ESR). The hydrogel samples of known weight (W1) were dried in a vacuum oven at 45 °C until constant weight (W2) was obtained. After drying, the hydrogels were washed with DI water by continuous water extraction for 12 h. The extracted hydrogels were dried at the same temperature in the vacuum oven until a constant weight was observed (W3). The GF of the hydrogel was calculated as the ratio W3/W2, and ESR was calculated using ESR = (W1-W3)/W3

Supporting Information

Supporting Information is available from the Wiley Online Library or from the author.

Acknowledgements

A.M. Abdelkader and A.R. Kamali appreciate the financial support received from the British Council Partnership Fund (CNBJS1). A.R.

Kamali appreciates the financial support received from the Fundamental Research Funds for the Central Universities, China (N2025001), and the National Natural Science Foundation of China (52250610222).

Conflict of Interest

The authors declare no conflict of interest.

Data Availability Statement

The data that support the findings of this study are available from the corresponding author upon reasonable request.

Keywords

intrinsic healing, nanocomposites, self-healing hydrogel, thiol modification, transition metal dichalcogenide, tungsten disulfide

Received: November 14, 2022
Revised: February 10, 2023
Published online: March 1, 2023

[1] R. J. Young, M. Liu, I. A. Kinloch, S. Li, X. Zhao, C. Vallés, D. G. Papageorgiou, *Compos. Sci. Technol.* **2018**, *154*, 110.
[2] M. Rahaman, R. Theravalappil, S. Bhandari, L. Nayak, P. Bhagabati, 4 – Electrical conductivity of polymer-graphene composites. In: Polymer Nanocomposites Containing Graphene: Woodhead Publishing (Eds.: M. Rahman, L. Nayak, I. A. Hussein, N. C. Das), **2022**. p. 107–39.
[3] B. Yuan, Y. Hu, X. Chen, Y. Shi, Yi Niu, Y. Zhang, S. He, H. Dai, *Composites, Part A* **2017**, *100*, 106.
[4] H.-P. Cong, P. Wang, S.-H Yu, *Chem. Mater.* **2013**, *25*, 3357.
[5] Y. Eom, S.-M. Kim, M. Lee, H. Jeon, J. Park, E. S. Lee, S. Y. Hwang, J. Park, D. X. Oh, *Nat. Commun.* **2021**, *12*, 621.
[6] C. R. Ratwani, A. R. Kamali, A. M Abdelkader, *Prog. Mater. Sci.* **2023**, *131*, 101001.
[7] C. I. Idumah, S. R Odera, *Polym. Plast. Technol. Mater.* **2020**, *59*, 1167.
[8] S. Wang, Z. Zhang, B. Chen, J. Shao, Z. Guo, *J. Appl. Polym. Sci.* **2018**, *135*, 46143.
[9] D. Lembke, S. Bertolazzi, A. Kis, *Acc. Chem. Res.* **2015**, *48*, 100.
[10] R. Kumar, W. Zheng, X. Liu, J. Zhang, M. Kumar, *Adv. Mater. Technol.* **2020**, *5*, 1901062.
[11] E. Singh, P. Singh, K. S. Kim, G. Y. Yeom, H. S Nalwa, *ACS Appl. Mater. Interfaces* **2019**, *11*, 11061.
[12] Y.-P. Gao, X. Wu, K.-J. Huang, L.-L. Xing, Y.-Y. Zhang, L. Liu, *CrystEngComm* **2017**, *19*, 404.
[13] P. Prabhu, V. Jose, J.-M Lee, *Matter* **2020**, *2*, 526.
[14] M. J. G. Guimarey, J. L. Viesca, A. M. Abdelkader, B. Thomas, A. Hernández Battez, M. Hadfield, *J. Mol. Liq.* **2021**, *342*, 116959.
[15] M. J. G. Guimarey, A. M. Abdelkader, M. J. P. Comuñas, C. Alvarez-Lorenzo, B. Thomas, J. Fernández, M. Hadfield, *Nanotechnology* **2021**, *32*, 025701.
[16] A. V. Menon, G. Madras, S. Bose, *ACS Appl. Polym. Mater.* **2019**, *1*, 2417.
[17] L. Bai, Y. Lei, H. Huang, Y. Liang, H. Yang, *Chem. Eng. J.* **2021**, *425*, 131450.
[18] S. Karunakaran, S. Pandit, B. Basu, M. De, *J. Am. Chem. Soc.* **2018**, *140*, 12634.
[19] X. Chen, N. C. Berner, C. Backes, G. S. Duesberg, A. R McDonald, *Angew. Chem., Int. Ed.* **2016**, *55*, 5803.
[20] H. R. Gutiérrez, N. Perea-López, A. L. Elías, A. Berkdemir, B. Wang, R. Lv, F. López-Urías, V. H. Crespi, H. Terrones, M. Terrones, *Nano Lett.* **2013**, *13*, 3447.
[21] A. Ennaoui, K. Diesner, S. Fiechter, J. H. Moser, F. Lévy, *Thin Solid Films* **1997**, *311*, 146.
[22] A. Berkdemir, H. R. Gutiérrez, A. R. Botello-Méndez, N. Perea-López, A. L. Elías, C.-I. Chia, B. Wang, V. H. Crespi, F. López-Urías, J.-C. Charlier, H. Terrones, M. Terrones, *Sci. Rep.* **2013**, *3*, 1755.
[23] X. Zhang, X.-F. Qiao, W. Shi, J.-B. Wu, D.-S. Jiang, P.-H Tan, *Chem. Soc. Rev.* **2015**, *44*, 2757.
[24] M. A. Pimenta, E. del Corro, B. R. Carvalho, C. Fantini, L. M Malard, *Acc. Chem. Res.* **2015**, *48*, 41.
[25] Z. Yu, Y. Pan, Y. Shen, Z. Wang, Z.-Y. Ong, T. Xu, R. Xin, L. Pan, B. Wang, L. Sun, J. Wang, G. Zhang, Y. W. Zhang, Yi Shi, X. Wang, *Nat. Commun.* **2014**, *5*, 5290.
[26] K. Cho, M. Min, T.-Y. Kim, H. Jeong, J. Pak, J.-K. Kim, J. Jang, S. J. Yun, Y. H. Lee, W.-K. Hong, T. Lee, *ACS Nano* **2015**, *9*, 8044.
[27] J.-S. Kim, H.-W. Yoo, H. O. Choi, H.-T Jung, *Nano Lett.* **2014**, *14*, 5941.
[28] K. C. Knirsch, N. C. Berner, H. C. Nerl, C. S. Cucinotta, Z. Gholamvand, N. Mcevoy, Z. Wang, I. Abramovic, P. Vecera, M. Halik, S. Sanvito, G. S. Duesberg, V. Nicolosi, F. Hauke, A. Hirsch, J. N. Coleman, C. Backes, *ACS Nano* **2015**, *9*, 6018.
[29] John Wiley & Sons I. SpectraBase, SpectraBase Compound ID = HNBVeUBMPEv, https://spectrabase.com/compound/HNBVeUBMPEv.
[30] H. C. Yau, M. K. Bayazit, J. H. G. Steinke, M. S. P Shaffer, *Chem. Commun.* **2015**, *51*, 16621.
[31] S. Kuldeep, O. Anil, S. K Dhawan, Polymer-Graphene Nanocomposites: Preparation, Characterization, Properties, and Applications, In: *Nanocomposites* (Ed.: E. Farzad), IntechOpen, Rijeka **2012**.
[32] B. Du, Yi Chao, K. Yang, B. Li, R. Luo, S. Zhou, H. Li, *AIP Adv.* **2022**, *12*, 095206.
[33] L. Chen, J. Shao, Q. Yu, S. Wang, *J. Dispersion Sci. Technol.* **2022**, *43*, 690.
[34] J. L. Suter, R. C. Sinclair, P. V Coveney, *Adv. Mater.* **2020**, *32*, 2003213.
[35] D. M. Sim, M. Kim, S. Yim, M.-J. Choi, J. Choi, S. Yoo, Y. S. Jung, *ACS Nano* **2015**, *9*, 12115.
[36] A. Ghorai, A. Midya, R. Maiti, S. K Ray, *Dalton Trans.* **2016**, *45*, 14979.
[37] A. Sajedi-Moghaddam, E. Saievar-Iranizad, *Mater. Res. Express* **2018**, *5*, 015045.